

# An adiabatic homogeneous model for the flow around a multi-perforated plate

S. Mendez \*

*CERFACS, 31057 Toulouse, France.*

F. Nicoud<sup>†</sup>

*University Montpellier II, CC51, I3M CNRS UMR 5149.*

*Place Eugène Bataillon. 34095 Montpellier, France.*

An adiabatic model to account for multi-perforated liners in combustion chamber flow simulations is described. It is separated into a suction model and an injection model to reproduce the average effect of effusion cooling on both sides of the plate. This model has been specifically designed to be used in industrial full-scale computations of gas turbine combustion chambers, where effusion cooling is commonly used for cooling the liners. Notably, it does not impose any minimal resolution at the wall and can be used with a coarse grid, the real perforated plate being replaced by a homogeneous boundary condition where the model is applied. From the analysis of former wall-resolved Large-Eddy Simulations (LES), the model is derived to conserve the wall fluxes. Two series of validations are proposed: *a priori* tests, where the model is compared with wall-resolved LES data and *a posteriori* tests, where an experimental test rig is computed replacing the perforated plate of the experiment by the model proposed in the paper. Conserving the wall fluxes allows reproduction of the global structure of the flow and leads to reasonable comparisons with experimental data.

## Nomenclature

$C_D$  Discharge coefficient through the plate

---

\*Post-doctoral fellow

<sup>†</sup>Professor. E-mail: franck.nicoud@univ-montp2.fr

$d$	Aperture diameter, $m$
$\vec{e}_x$	Unit vector in the streamwise direction
$\vec{e}_y$	Unit vector in the vertical direction
$h$	Channel height, $m$
$\vec{n}$	Outward normal vector
$P$	Pressure, $Pa$
$q$	Mass flow rate through one hole, $kg/s$
$Re$	Reynolds number
$S$	Wall surface
$T$	Temperature, $K$
$U_1$	Streamwise velocity at the center of channel 1
$U_2$	Streamwise velocity at the center of channel 2
$U$	Streamwise velocity, i.e. $V_1$
$V_i$	$i$ th component of the velocity vector
$V_j$	Bulk velocity in the hole, $m/s$
$V$	Vertical velocity, i.e. $V_2$
$W$	Spanwise velocity, i.e. $V_3$
$x_i$	$i$ th coordinate
$x$	Streamwise coordinate, i.e. $x_1$
$y$	Vertical coordinate, i.e. $x_2$
$z$	Spanwise coordinate, i.e. $x_3$
$\alpha$	hole angle with respect to the wall
$\delta_{ik}$	Kronecker symbol 1 if $i = k$ , 0 else
$\Phi(X)$	Wall flux per unit surface of quantity $X$
$\varphi$	Mass flow rate per total surface unit $\frac{q}{S_w}$ , $kg/s/m^2$
$\rho$	Mass density, $kg/m^3$
$\sigma$	Porosity
$\tau_{ik}$	Viscous stress tensor $\mu(\frac{\partial V_i}{\partial x_k} + \frac{\partial V_k}{\partial x_i}) - \frac{2}{3}\mu\frac{\partial V_l}{\partial x_l}\delta_{ik}$
<i>Subscript</i>	
1	Relative to channel 1 (injection channel)
2	Relative to channel 2 (suction channel)
$h$	Relative to the hole
$jet$	Relative to the jet
$out$	Relative to the first off-wall grid point
$s$	Relative to the solid part of the perforated plate
$W$	Relative to the total perforated plate (aperture and solid part)

*wall* Relative to a grid point located at the wall

*Superscript*

*inj* Relative to the injection side

*suc* Relative to the suction side

## I. Introduction and objectives

In gas turbines, the turbine blades and the liner of the combustion chamber are submitted to large thermal constraints. As the materials used for these solid parts cannot stand such high temperature and temperature gradients, they need to be cooled. As pointed out by Lefebvre,<sup>1</sup> the most efficient cooling system is transpiration-based: the solid parts to be cooled are made of porous material through which cool air is injected. The resulting uniform film of fresh gas isolates the solid parts from the hot products. However, the application of transpiration in gas turbines is not practical due the mechanical weakness of available porous materials and alternative technological solutions are sought for. One possibility often chosen for combustion chamber liners is to use multi-perforated walls to produce the necessary cooling. In this approach (see Fig. 1), fresh air coming from the casing goes through thousands of angled perforations and enters the combustion chamber. This is a discrete form of transpiration cooling: the cooling film that protects the liner from the hot gases results from the coalescence of the discrete micro-jets emanating from the perforations. This technique is usually called full-coverage film cooling (FCFC) to distinguish it from the film cooling (FC) systems used for turbine blades, where only a few cooling holes are required.

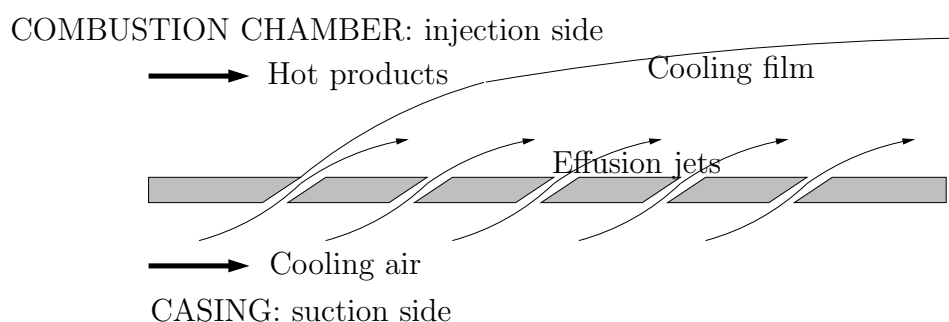


**Figure 1. Principle of full-coverage film cooling: fresh air flowing in the casing is injected into the combustion chamber through the liner perforations and forms an isolating film protecting the internal face of the liner from the combustion gases.**

When computing the 3-D turbulent reacting flow within the burner, the number of sub-millimetric holes is far too large to allow a complete description of the generation and coales-

cence of the jets. This is particularly true for the Reynolds-Averaged Navier-Stokes (RANS) computations used by the industrial manufacturers to design their combustion chambers. However, effusion cooling cannot be neglected: it is known to have drastic effects on the whole flow structure, notably by changing the flame position and subsequently modifying the temperature field. An appropriate model is then needed to reproduce the effect of effusion cooling on the main flow. Such a modeling effort has already been done for transpired boundary layers and extended law-of-the-wall for moderate uniform blowing or suction are available.<sup>2,3</sup> It is quite obvious that for a given injected mass flow rate, the injected momentum flux is different depending on if the injection is done through a porous material (uniform injection) or a perforated plate (discrete injection). As a consequence, existing models accounting for moderate transpiration can hardly be adapted to FCFC and new wall models for turbulent flows with effusion are required to perform predictive full-scale computations. The purpose of the present paper is to propose a simple model, independent of the grid in the near-wall region, to account for effusion through a multi-perforated plate: this model has to deal with both sides of the perforated plate, as the current trend in industrial computations is to include the casing when dealing with combustion chambers.

The design of such models needs to be supported by detailed data concerning FCFC. Several academic configurations are related with FCFC problems. The suction of a boundary layer through one or several perforations is not highly documented<sup>4</sup> and the flow at the suction side is rarely considered in details in the studies concerning injection through short holes.<sup>5,6</sup> From the injection side, the cooling jets can be seen as an array of jets in crossflow (JCF). Contrary to suction, JCF have been widely studied over the years because of their high engineering interest (see for example the review by Margason<sup>7</sup>) and continue to be a subject of active research.<sup>5,8-11</sup> Note however that the FCFC jets differ from the most common configurations of jets in crossflow in several aspects: while single canonical JCF are usually designed to penetrate in the main flow and enhance mixing, the purpose of effusion jets is to create a film in order to protect the wall from hot gases: many jets are used to form this film, and they are oriented so that the cooling air stays next to the wall. The inclination of the jets in FCFC application is thus smaller than in JCF, modifying the penetration of the jets as well as the interaction with the upstream main flow,<sup>12,13</sup> Furthermore, in FCFC, the crossflow is not a simple boundary layer as for JCF studies; it results from the interaction between all the jets upstream. At last, owing to the small length-to-diameter ratio of the holes in FCFC applications, the flow in the injection side is strongly related to the flow in the aperture and in the suction side.<sup>5,14,15</sup>

In view of these differences, extrapolating the results from JCF studies to gain insight into FCFC would not be justified and specific FCFC configurations must be considered. This is also what Walters and Leylek<sup>15</sup> state by insisting on the importance of reproducing the ex-

act geometry for film cooling studies. However, generating this type of data experimentally is very challenging: the operating conditions in the combustion chambers (high temperature and high pressure) are difficult to reproduce in test rigs and experimental techniques are rarely adapted to such conditions. Moreover, the characteristic size of the micro-jets being sub-millimetric, the main flow features are out of reach of current measurements techniques. This explains the lack of detailed measurements in realistic operating conditions: accurate information about the velocity field in FCFC configurations is available only on large-scale isothermal plates.<sup>16-18</sup> When experiments are performed on plates at real scale, only wall parameters,<sup>19-22</sup> like the heat transfer coefficient or the adiabatic cooling efficiency, or integrated data like the discharge coefficient<sup>23,24</sup> are provided and very often, only small temperature differences between the hot and the cold streams are investigated.

The alternative is to rely on accurate direct simulations to generate the requested data. However requirements in computational power are huge due to the configuration: in FCFC, the perforated plate contains hundreds or thousands of holes and resolving the flow in each of these holes would be very expensive. To overcome this difficulty, Mendez *et al.*<sup>25,26</sup> derived a numerical methodology where only one aperture is resolved and periodic conditions are prescribed in the directions parallel to the plate, thus representing the asymptotic case of an infinite perforated plate. This approach proved suitable to provide insight regarding the flow structure in the case of FCFC.<sup>27</sup> In this paper, these simulations are referred to as the "reference small-scale simulations".

The present paper details the methodology developed for post-processing the reference isothermal data obtained by Large Eddy Simulations (LES)<sup>27</sup> and proposes a homogeneous model that accounts for the major flow characteristics near a perforated wall. In this model, the injection and the suction sides are coupled, a law for the discharge coefficient in the holes relating the pressure drop to the mass flow rate through the plate. The inputs are the pressure drop across the plate and the geometrical characteristics (porosity, aperture angle). *A priori* testing is first performed, the fluxes provided by this homogeneous model being compared to the reference simulations. As an *a posteriori* validation, the model is implemented in a LES code in order to reproduce an experimental set-up where two channels are separated by a perforated plate. Numerical results are compared with experimental measurements performed in an isothermal large-scale configuration.<sup>18</sup>

An analysis of small-scale LES results<sup>27</sup> is provided in section II, in order to estimate the fluxes at the perforated plate: an adiabatic model for effusion cooling is constructed from this analysis. This model is then used to compute an academic isothermal flow configuration already investigated experimentally.<sup>18</sup> Section III describes the numerical code used to perform the *a posteriori* simulations, as well as the experimental configuration.<sup>18</sup> Eventually, the performances of the homogeneous model are assessed by providing comparisons with the

available experimental data in section IV. The homogeneous model is also compared with a simpler one, imposing the spatial-averaged velocity at wall.

## II. Construction of a model for effusion cooling from LES results

To perform fast-running simulations of their combustion chambers in presence of effusion cooling, manufacturers need a model that reproduces the main effects of effusion on the main flow. This model must meet several criteria:

- It has to provide information about both sides of the plate. Indeed, the current trend is to include the casing when computing the flow in a combustion chamber, in order to avoid prescribing the repartition of air injection a priori; thus both the casing side (suction of cooling air) and the combustion chamber side (injection of this cooling air) must be modeled,
- As the objective is to use coarse grids to decrease the running time, the flow near the wall would not be resolved: effusion through small holes ( $d \approx 0.5 \text{ mm}$ ) imposes characteristic length scales that cannot be solved over coarse meshes. As a consequence, the model must represent the multi-perforated plate as a homogeneous boundary, without distinction between perforations and solid parts of the wall,
- The model has to be local. Global parameters, such as the number of upstream rows, are often used for models related to effusion cooling (see for example Mayle and Camarata<sup>28</sup> for a model of the adiabatic effectiveness of the cooling). However, in a combustion chamber, the row number cannot always be defined, and the notion of upstream direction is a fuzzy concept in 3-D geometries with multiple inlets/outlets. To overcome this problem, the model should only require information from the flow in the neighborhood of each point where it is to be used.

To satisfy these criteria, the objective is to build a uniform model that only has local information as input data, and that reproduces correctly the fluxes at both sides of the perforated wall: this is inspired by what is done for wall-function boundary conditions for impermeable walls, where the wall friction and the wall heat flux are assessed in order to reproduce the macroscopic effect of the solid boundary on the main flow. The following sub-section aims at describing the reference simulations and their post-treatment in order to construct such a model.

## A. Analysis of the small-scale reference LES results

Small-scale simulations were performed in order to learn more about the fine structure of the flow around and inside a perforated plate in an isothermal configuration corresponding to the LARA experiment. A complete description of the methodology can be found in Mendez et al.<sup>25</sup> while advanced analysis of the results is available in Mendez and Nicoud.<sup>27</sup> In FCFC experiments, the flow is known to be different depending on the number of rows of perforations considered. This is very difficult to handle from a modeling point of view. Furthermore, as already said, this dependence on the row number cannot be transposed to complex geometries. This is the reason why the case where the perforated plate is infinite was considered for generating the reference LES data. The computational domain can then be reduced to a small box containing only one perforation, using periodic boundary conditions in order to reproduce the periodicity of the staggered pattern. This is also consistent with the construction of a local model where only local information should be used. The calculation domain is presented in figure 2. The aperture of diameter  $d = 5 \text{ mm}$  is angled at  $\alpha = 30^\circ$  with the plate, in the streamwise direction, without any spanwise orientation. The thickness of the plate being 10 mm and holes being angled at  $30^\circ$  with the plate, the hole length-to-diameter ratio is 4. The diagonals of the computational domain are  $z = 0$  and  $x = 0$  and their lengths equal the hole-to-hole distance, viz.  $11.68 d$  in the streamwise direction ( $z = 0$ ) and  $6.74 d$  in the spanwise direction ( $x = 0$ ). The center of the hole is located at  $x = 0$ ,  $y = 0$ ,  $z = 0$  for the injection side (hole outlet) and at  $x = 3.46 d$ ,  $y = 2 d$ ,  $z = 0$  for the suction side (hole inlet). The calculation grid contains 25,000,000 tetrahedral cells: 45 points

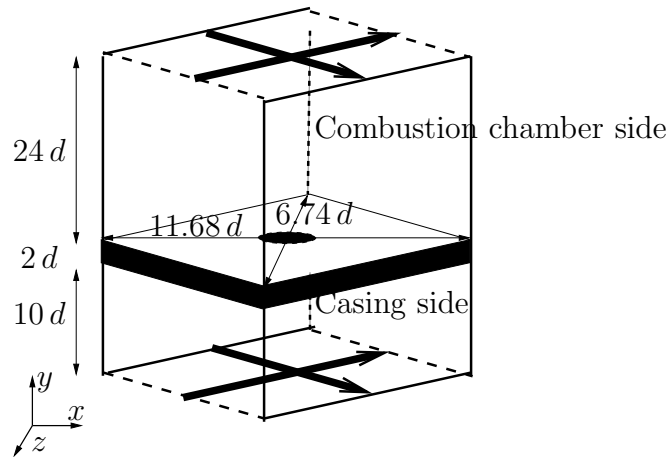


**Figure 2. Calculation domain centered on a perforation; the bold arrows correspond to the periodic directions. The computational domain dimensions are provided.**

describe the diameter of the hole and, on the average, the first off-wall point is located 2 wall units apart from the wall. Typically the cells along the wall to be cooled and in the hole are sized to a height of 0.11 mm.

A pressure drop of 41 Pa is effectively imposed in the simulation. The resulting bulk velocity in the hole is  $V_j \approx 5.84 \text{ m s}^{-1}$  and the mass flow rate through the hole is  $q = 0.129 \text{ g s}^{-1}$ . Note that the mass density is approximately constant, with  $\rho \approx 1.13 \text{ kg m}^{-3}$ . These values of mass density and velocity,  $\rho$  and  $V_j$ , are used as reference for non-dimensional quantities. The geometric and aerodynamic characteristics of the simulations were tuned to reproduce the operating conditions of an experimental setup named LARA, described further in section IIIB.

The simulations in such a periodic configuration have proved to provide results that reproduce very well the global structure of the flow observed in the LARA experiment and comparisons with experimental profiles at row 9 show good agreement.<sup>27</sup> The numerical fields have been averaged over 20 flow through times (FTT). This time-averaged solution of the flow is analyzed here in terms of wall modeling. A complete analysis of these data can be found in Mendez and Nicoud.<sup>27</sup> Time-averaged quantities are denoted by the  $\bar{\cdot}$  operator.

The model has to reproduce correctly the momentum and energy fluxes at the perforated plate (injection and suction sides) at a given mass flow rate and geometry. Indeed, the mass flow rate through the plate is supposed to be known: it is either imposed by the user, or it can be calculated thanks to a relationship between the pressure drop and the mass flow rate thanks to a discharge coefficient, in cases where both sides of the plate are computed. The analysis of small-scale data can support the modeling effort by answering to two main questions:

- Among the terms contributing to the wall fluxes, which are the dominant ones?
- The mass flow rate being known, is it possible to model the dominant fluxes?

Note that because the flow computed is isothermal, only information about the momentum fluxes at the perforated plate are relevant. Momentum fluxes are calculated over two planes located just above (for the injection side) and below (for the suction side) the perforated plate (see Fig. 3). The perforated plate is considered as a boundary made of two parts: the hole surface ( $S_h$ ) and the solid surface ( $S_s$ ). The normal to the total surface, taken in the outward direction from the fluid point of view, is noted  $\vec{n}$ .

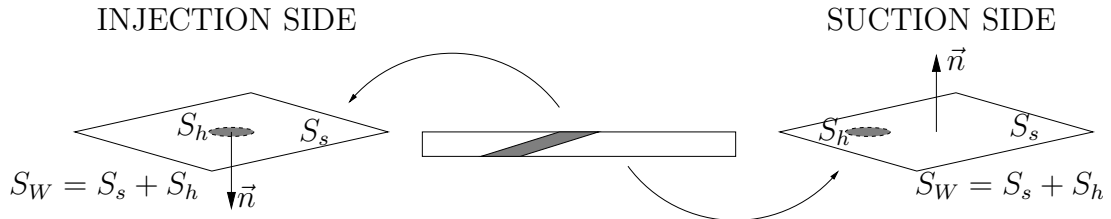


**Figure 3. Schematic of the planes where the fluxes are assessed.**

From the momentum conservation equation, both the viscous ( $\tau_{ik}$ ,  $k = 1, 2, 3$ ) and the inviscid ( $P\delta_{ik} + \rho V_i V_k$ ,  $k = 1, 2, 3$ ) terms contribute to the flux associated to the momentum in the  $x_i$  direction. Furthermore, both the solid part and the aperture of the multi-perforated plate contribute to the global flux over the  $x-z$  planes represented in Fig. 3. The expressions of the different contributions are summarized in Table 1. In the configuration considered, the normal to the homogeneous boundary is along the  $y$ -direction:  $\vec{n} = -\vec{e}_y$  or  $n_2 = -1$  for the injection wall and  $\vec{n} = \vec{e}_y$  or  $n_2 = 1$  for the suction wall.

	solid wall		hole	
	viscous	non-viscous	viscous	non-viscous
$\overline{\rho V}$	$\int_{S_s} \overline{\tau_{22}} n_2 dx dz$	$\int_{S_s} (-\overline{P}) n_2 dx dz$	$\int_{S_h} \overline{\tau_{22}} n_2 dx dz$	$\int_{S_h} (-\overline{P} - \overline{\rho V^2}) n_2 dx dz$
$\overline{\rho V_{t_i}}$	$\int_{S_s} \overline{\tau_{i2}} n_2 dx dz$	0	$\int_{S_h} \overline{\tau_{i2}} n_2 dx dz$	$\int_{S_h} (-\overline{\rho V V_{t_i}}) n_2 dx dz$

**Table 1.** Contributions to the momentum fluxes over a  $x-z$  plane just above (injection side  $n_2 = -1$ ) or just below (suction side  $n_2 = +1$ ) the perforated plate.  $V_{t_i}$  is U or W ( $i = 1$  or 3).

Small-scale computations allow to assess the different terms of the momentum fluxes on the suction and injection wall planes. Integrations over the solid wall ( $S_s$ ) and the hole surface ( $S_h$ ) are performed and the results are reported in Tables 2 and 3 for the streamwise and vertical momentum respectively. Viscous fluxes have not been reported in Table 3 (vertical momentum), as they are negligible compared to inviscid contributions.

Region	total plate	hole		solid wall
Expression	$\int_{S_W} (-\overline{\rho U V} + \overline{\tau_{12}}) n_2 dx dz$	$\int_{S_h} -\overline{\rho U V} n_2 dx dz$	$\int_{S_h} \overline{\tau_{12}} n_2 dx dz$	$\int_{S_s} \overline{\tau_{12}} n_2 dx dz$
Injection	$7.21 \times 10^{-1}$	114.1	-0.1	-14.0
Suction	$-2.83 \times 10^{-1}$	86.8	0.0	13.2

**Table 2.** Wall fluxes for the streamwise momentum: First column: expression and values of the total flux (in  $\rho V_j^2 d^2$ ) on both sides of the plate (total surface  $S_W$ ). Columns 2–4: relative contributions (in %) of the terms involved in the wall fluxes.

Streamwise momentum  $\rho U$ : the non-viscous streamwise momentum flux is the main term for both the suction and the injection sides of the perforated plate. The viscous term over the hole surface is very small. The wall friction over the solid wall is approximately 10 times smaller than the non-viscous aperture term for the operating point considered. This means that one can only focus on the inviscid part of the flux when developing a (rough) model for effusion. In other words, assuming that the turbulent transfers scale as the wall friction, turbulence is not a first-order issue when dealing with discrete effusion, which is of course significantly different from the classical case of an attached boundary layer over a solid plate.

Vertical momentum  $\rho V$ : the flux of normal momentum involves a pressure term that is

Region	total plate	hole	solid wall
Expression	$\int_{S_W} (-\bar{P} - \overline{\rho V^2} + \overline{\tau_{22}}) n_2 dx dz$	$\int_{S_h} -(\bar{P} + \overline{\rho V^2}) n_2 dx dz$	$\int_{S_s} -\bar{P} n_2 dx dz$
Injection	$3.42 \times 10^3$	4	96
Suction	$-3.46 \times 10^3$	4	96

**Table 3. Wall fluxes for the vertical momentum: First column: expression and values of the total flux (in  $\rho V_j^2 d^2$ ) on both sides of the plate (total surface  $S_W$ ). Columns 2–5: relative contributions (in %) of the terms involved in the wall fluxes.**

clearly dominant. The velocity term in the hole is small compared to the pressure term. The repartition between hole and solid surface fluxes is completely related to the porosity of the plate  $\sigma = 0.04$ : pressure is almost constant over the whole wall.

Note that owing to the symmetry of the problem, the spanwise momentum flux should be zero. In the computation, it is not perfectly so but for injection the spanwise momentum flux is approximately 5000 times smaller than the streamwise momentum flux. This ratio is even smaller for the suction side.

An appropriate model has thus to reproduce the two main effects of the flow around a perforated plate: the non-viscous streamwise momentum flux due to injection and the non-viscous vertical momentum flux that can be reduced to the pressure term. All the other terms are negligible, at least in a first-order modeling effort.

## B. Construction of the uniform model for full-scale simulations

In this section, a uniform model is constructed for each side of the plate to reproduce the non-viscous streamwise momentum flux in the hole and the non-viscous vertical momentum flux. On the suction side, the model integrates an estimation of the wall friction.

### 1. Injection side

As observed in the analysis of the reference small-scale simulations, the non-viscous vertical momentum flux can be reduced to a pressure term. The wall pressure should thus be evaluated at the wall. As it is usual in wall-bounded flows, we will consider that the outer pressure is a good measure of the pressure in the vicinity of the wall. This is verified in the small-scale LES results, as shown in figure 4. Time-averaged pressure is averaged over horizontal  $(x, z)$  planes and displayed as a function of the vertical coordinate  $y$ . Compared to the pressure drop across the plate, the variations of the time and spatial averaged pressure profile in each channel is less than 1%. It is approximately equal to  $\rho V_j^2 \sigma (1 - \sigma) / 4$  (difference in the dynamic pressure at the perforated plate and far from it).

Thus, the pressure term of the vertical momentum flux at the wall can be easily related to the first off-wall pressure values obtained in a coarse grid combustion chamber calculation.

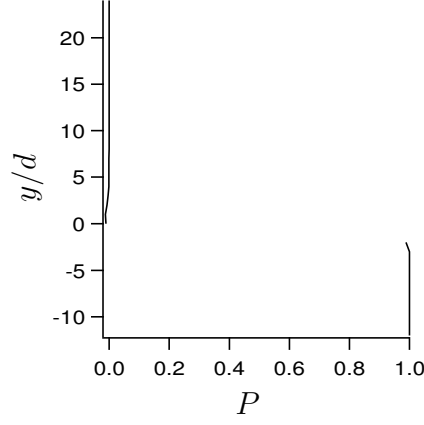


**Figure 4.** Time and spatial averaged pressure vertical profile in the calculation domain (except the aperture) as a function of  $y$ . Pressure is dimensionless:  $P = 0$  at the upper limit and  $P = 1$  at the lower limit of the domain.

As can be seen in figure 4, this stands for each side the plate, and the assessment of the pressure at the wall from the outer pressure will also be used on the suction side.

Hence, the main modeling effort consists in obtaining a good estimation of the non-viscous streamwise momentum flux in the hole. We are going to present the model in terms of equivalent boundary condition, answering the following question: what is the equivalent injection over the whole plate surface that better represents the real injection of fluid through cooling holes.

Before constructing a homogeneous model over the whole surface, it proves useful to consider a preliminary model where the velocity components take two different values, one related to the aperture,  $\overrightarrow{V}_h^{inj}$ , the other to the solid part of the plate, where the classical condition  $\overrightarrow{V}_s^{inj} = \vec{0}$  is imposed, as represented in Fig. 5. The wall-normal vertical velocity

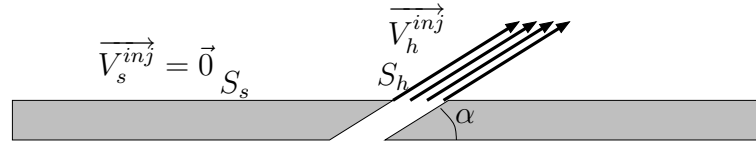


**Figure 5.** Principle of the intermediate model: separation into two zones of constant velocity values. Example for the injection side.

to impose for the aperture is directly related to the mass flow rate, but the tangential components are *a priori* unknown. To determine them, it is assumed that at the hole outlet, the direction of the jet is imposed by the aperture angle  $\alpha$ . Thus, the intermediate model we propose reads:

$$V_h^{inj} = V_j \sin(\alpha) = \frac{q}{S_h \rho} \quad \text{over } S_h \quad \text{and} \quad V_s^{inj} = 0 \quad \text{over } S_s, \quad (1)$$

$$U_h^{inj} = V_j \cos(\alpha) \quad \text{over } S_h \quad \text{and} \quad U_s^{inj} = 0 \quad \text{over } S_s. \quad (2)$$

The inviscid flux of streamwise momentum can be assessed from Eq. 1 and 2 and compared to the numerical results obtained in the reference simulations.<sup>27</sup> From the above intermediate model, the inviscid flux of streamwise momentum at the injection side is

$$\rho \frac{V_j^2 \sin^2(\alpha)}{4 \tan(\alpha)} \frac{\Pi d^2}{4 \sin(\alpha)}$$

which gives a non dimensional value of  $\Pi \cos(\alpha)/4 \approx 0.680$ . This value of 0.680 must be compared to the value of 0.823 (114.1% of 0.721, see table 2) in the reference simulation.

From the analysis of the reference numerical database,<sup>27</sup> it appears that the errors of this crude model have two main sources:

- the flat profile assumption, viz. the approximation of the flow in the hole by constant values of velocity. Implicitly, it has been considered that:

$$\frac{1}{S_h} \int_{S_h} \overline{\rho U V} ds = \left( \frac{1}{S_h} \int_{S_h} \bar{\rho} ds \right) \left( \frac{1}{S_h} \int_{S_h} \bar{U} ds \right) \left( \frac{1}{S_h} \int_{S_h} \bar{V} ds \right). \quad (3)$$

This equality is almost verified on the injection side of the plate but it introduces an error of approximately 10% on the evaluation of the streamwise momentum flux. Mendez and Nicoud<sup>27</sup> showed that this error is due to the strong spatial correlation between the time-averaged  $U$  and  $V$  fields at the perforation outlet section. It is interesting to note that neglecting the temporal fluctuations has a very small impact on the modeling errors.

- the estimation of the tangential velocity (here the streamwise velocity): the assumption that the geometrical angle ( $\alpha$ ) is also relevant to the velocity vector at the injection side is not perfectly true. Assuming that  $U_h^{inj} = V_h^{inj} \cotan(\alpha)$  (Eq. 2) at the hole outlet introduces an error of 10% on the estimation of the streamwise velocity at the hole outlet: the jet angle in the reference simulation is  $28^\circ$  instead of  $30^\circ$  for the hole angle.

Eventually, the model described by Eq. 1 and 2 assesses the inviscid streamwise momentum flux on the injection side of the plate with an error of 20%. This error is not small but is considered to be acceptable, given the simplicity of the model.

The aim is now to design a homogeneous condition that applies over the entire surface of the plate and that has the same characteristics in terms of resulting momentum fluxes. As stated before, the objective is to provide a FCFC model for simulations involving a perforated plate without resolving the flow inside and near the plate. The model for FCFC has thus to

be homogeneous to be adapted to any grid in the near-wall region: the holes and the solid wall are not distinguished. This means that the mass flow rate is injected through the entire plate and that the injection surface is  $1/\sigma$  larger in the homogeneous model than in the actual situation where only the aperture contributes to the fluid injection. As a consequence the normal injection velocity is multiplied by  $\sigma$  to ensure that the proper mass flow rate crosses the equivalent boundary.

In order to retrieve the same streamwise momentum flux as the inhomogeneous model of Eq. 1 and 2, a homogeneous model is proposed, with a modified injection angle  $\alpha'$ :

$$V_W^{inj} = \sigma \frac{q}{S_h \rho} \quad \text{over} \quad S_W, \quad (4)$$

$$U_W^{inj} = V_W^{inj} \cotan(\alpha') \quad \text{over} \quad S_W. \quad (5)$$

( $\alpha'$ ) is directly related to ( $\alpha$ ) through:  $\tan(\alpha') = \tan(\alpha)\sigma$ . This homogeneous injection model injects the same mass flow rate as the model of Eq. 1 to 2 but the angle of injection is modified to ensure proper streamwise momentum flux through the plate. Note also that this model does not allow reproducing the vertical momentum flux corresponding to Eq. 1 to 2. However, as the vertical momentum flux is dominated by a pressure term that is correctly evaluated from the outer pressure, the difference is negligible between the intermediate model and the homogeneous model.

## 2. Suction side

As stated before (see figure 4), the vertical non-viscous momentum flux at the wall on the suction side can be evaluated from the outer pressure (pressure at the first-off wall). Moreover, as the model we are seeking for is homogeneous, the vertical velocity at the wall must be constant and defined in such a way that the mass flux is properly reproduced. Note that the value is the same as at the injection side of the plate.

$$V_W^{suc} = V_W^{inj} = \sigma \frac{q}{S_h \rho} \quad \text{over} \quad S_W. \quad (6)$$

The streamwise velocity at the suction wall that is unknown is going to be determined directly (without using an intermediate model) from the flow characteristics at the first off-wall point in the suction channel. The mesh point at the wall is noted  $N_{wall}^{suc}$  and the first off-wall mesh point is noted  $N_{out}^{suc}$ . Assuming a steady state and an equilibrium between the wall and the first off-wall point, a streamwise momentum balance is written (Eq. 7) using a control volume closed by two surfaces parallel to the wall:  $\Sigma_{wall}$  at the wall and  $\Sigma_{out}$  at the level of  $N_{out}^{suc}$ .  $\Sigma_{wall}$  is considered to be large enough to include several holes (see Fig. 6).

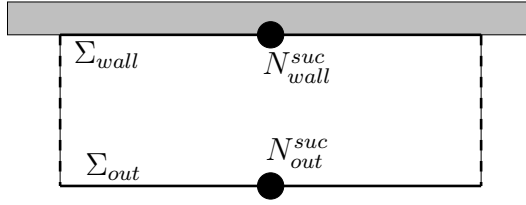


**Figure 6.** Definition of surfaces for the momentum balance of Eq. 7.

$$\int_{\Sigma_{wall}} (\overline{\rho U V} - \overline{\tau_{12}}) ds = \int_{\Sigma_{out}} (\overline{\rho U V} - \overline{\tau_{12}}) ds. \quad (7)$$

At the wall,  $\tau_{12}$  is essentially the solid wall friction, whereas  $\tau_{12}$  at the height of node  $N_{out}^{suc}$  (over  $\Sigma_{out}$ ) represents all the diffusion terms at the first off-wall point. It is the sum of laminar diffusion and either sub-grid diffusion (in LES) or turbulent diffusion (in RANS computations). In the reference small-scale simulations, Eq. 7 is exact, as the equilibrium state is reached and periodicity is assumed. The left-side of Eq. 7 corresponds to the total streamwise momentum flux at the suction side of the wall. From the evaluation of the streamwise fluxes at node  $N_{out}^{suc}$ , it is thus possible to estimate the total streamwise momentum flux at the suction side of the wall. The model used for  $U$  is therefore

$$U_W^{suc} = U_{out}^{suc} - \frac{(\tau_{12})_{out}^{suc}}{\rho V} \quad \text{over } S_W, \quad (8)$$

with  $U_{out}^{suc}$  and  $\tau_{out}^{suc}$  the instantaneous values of velocity and wall shear stress at node  $N_{out}^{suc}$ . At the equilibrium, this velocity verifies Eq. 7. Note that contrary to the injection side, the model on the suction side stands for the total streamwise wall flux because the momentum budget can only be written for the sum of viscous and non-viscous contributions. It is considered that the streamwise momentum that is not lost through friction goes out of the suction channel through the hole inlet surface.

Eventually, the complete homogeneous model for discrete injection/suction reads:

$$V_W^{inj} = \sigma \frac{q}{S_h \rho} \quad \text{over } S_W, \quad (9)$$

$$U_W^{inj} = \sigma \frac{q}{S_h \rho} \cotan(\alpha') = \frac{q}{S_h \rho} \cotan(\alpha) \quad \text{over } S_W, \quad (10)$$

$$V_W^{suc} = V_W^{inj} = \sigma \frac{q}{S_h \rho} \quad \text{over } S_W, \quad (11)$$

$$U_W^{suc} = U_{out}^{suc} - \frac{(\tau_{12})_{out}^{suc}}{\rho V_W^{suc}} \quad \text{over } S_W. \quad (12)$$

The homogeneous model is completed by two assumptions: the spanwise velocity is zero

due to symmetry of the problem and the mass density of the fluid injected in the injection channel is considered to be equal to the mass density of the fluid entering the plate. The plate is thus considered to be adiabatic: the plate and the fluid do not exchange heat.

The performances of the model are summarized in Table 4. Momentum fluxes from the reference small-scale simulations<sup>27</sup> are compared with fluxes reconstructed from Eq. 9 to 12. Note that the model for the streamwise momentum flux over the suction wall stands for the total flux (non-viscous and viscous flux) whereas only the non-viscous part of the streamwise momentum flux is modeled on the injection side. Note also that the term  $\overline{\rho V^2}$  is under-estimated, but this has no impact on the model, as this term is negligible compared to the pressure term.

Fluxes	Contributions	Injection		Suction	
		Reference data	Model	Reference data	Model
$\phi(\rho U)$	$\overline{\rho U V}$	$8.23 \times 10^{-1}$	$6.80 \times 10^{-1}$	$-2.46 \times 10^{-1}$	$-2.83 \times 10^{-1}$
	$\overline{\tau_{12}}$	$-1.02 \times 10^{-1}$	0	$-3.74 \times 10^{-2}$	
$\phi(\rho V)$	$\overline{P}$	$3.42 \times 10^3$	$3.42 \times 10^3$	$-3.46 \times 10^3$	$-3.46 \times 10^3$
	$\overline{\rho V^2}$	$4.50 \times 10^{-1}$	$1.54 \times 10^{-2}$	$-5.46 \times 10^{-1}$	$-1.54 \times 10^{-2}$
	$\overline{\tau_{22}}$	$1.59 \times 10^{-4}$	0	$-2.71 \times 10^{-4}$	0
$\phi(\rho W)$	$\overline{\rho V W}$	$-4.61 \times 10^{-5}$	0	$1.16 \times 10^{-4}$	0
	$\overline{\tau_{32}}$	$-7.93 \times 10^{-5}$	0	$-9.21 \times 10^{-5}$	0

**Table 4.** *A priori* testing of the homogeneous model (Eq. 9 to 12): momentum wall fluxes on the injection and suction sides of the plate. Comparisons with the reference small-scale simulations. Values of fluxes in  $\rho V_j^2 d^2$ . The integration wall surface for the model corresponds to the one of the reference calculations.

### C. Implementation of the homogeneous model

Some details about the implementation of the model in a flow solver are given below in the framework of a cell-vertex method<sup>29</sup> where the unknowns are stored at the nodes of the mesh. A similar implementation can be done for cell-centered schemes where the unknowns are stored at the center of the cells (classical finite volumes). For sake of simplicity, one assumes that the surface meshes on the injection and the suction sides coincide (see Fig.7). To determine the operating conditions at a liner point, only the values at this node and at the corresponding node on the other side of the plate (same streamwise and spanwise coordinates on the other side) are used. At each iteration, the mass flow rate per surface unit through the plate,  $\varphi$ , is computed from the pressure drop across the liner, assessed as the difference between the nodal pressures  $P_{wall}^{inj}$  and  $P_{wall}^{suc}$  and the mass density in the

calculation, for example determined at  $N_{wall}^{suc}$ :  $\rho = \rho_{wall}^{suc}$  (see Fig. 7). For doing so,  $\varphi$  is related to the micro-jets velocity  $V_j$ , viz.  $\varphi = \rho V_j \sin(\alpha) \sigma$ . Introducing the discharge coefficient  $C_D$  to express  $V_j$  as a function of  $\Delta P = P_{wall}^{suc} - P_{wall}^{inj}$ , viz.  $\frac{1}{2} \rho V^2 = C_D^2 \Delta P$ , the mass flow rate per unit wall surface is then  $\varphi = \sin(\alpha) \sigma \sqrt{2\rho C_D^2 \Delta P}$ .

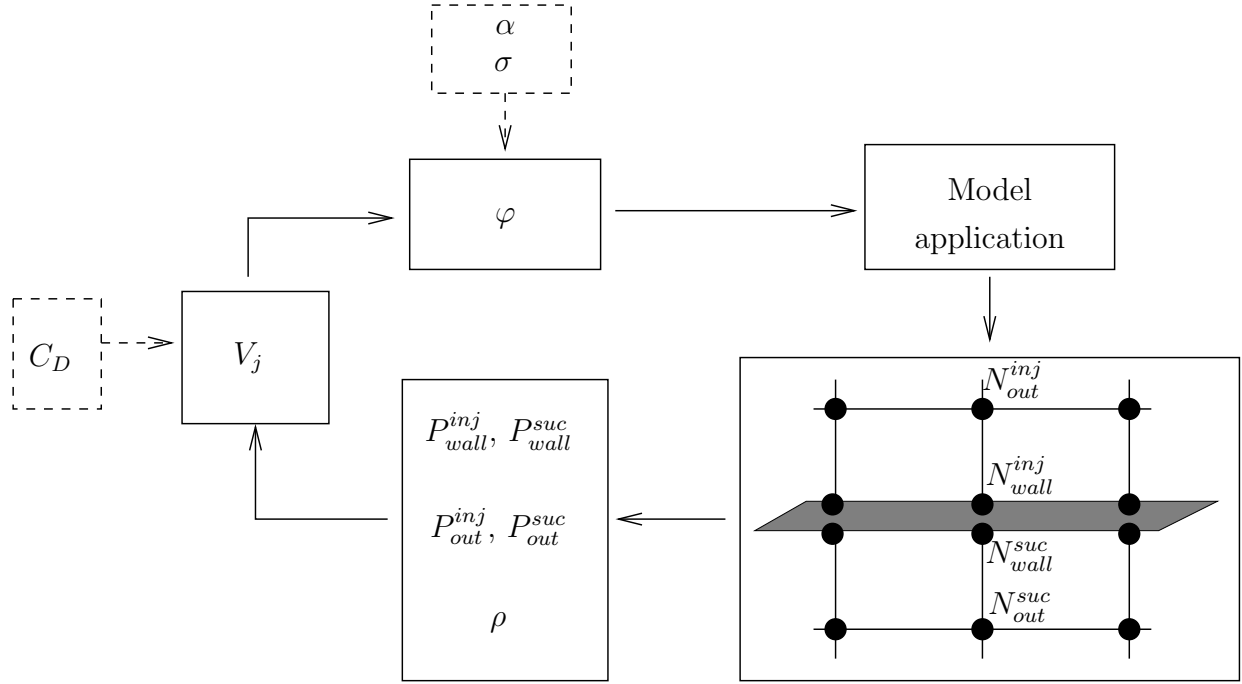


Figure 7. Schematic of the coupling procedure. Dotted lines denote the external input parameters needed by the model: only the geometrical details (porosity and hole angles) and a law for the discharge coefficient  $C_D$  must be provided.

Once  $\varphi$  is known, the following fluxes are imposed (box *Model application* in figure 7):

- at the suction side:

$$\Phi(\rho) = \rho V_W^{suc} = \varphi, \quad (13)$$

$$\Phi(\rho U) = \rho V_W^{suc} U_W^{suc} = \varphi U_{out}^{suc} - (\tau_{12})_{out}^{suc}, \quad (14)$$

$$\Phi(\rho V) = \rho (V_W)^2 + P_{out}^{suc} = \frac{\varphi^2}{\rho} + P_{out}^{suc}, \quad (15)$$

$$\Phi(\rho W) = 0. \quad (16)$$

- at the injection side:

$$\Phi(\rho) = \rho V_W^{inj} = \varphi, \quad (17)$$

$$\Phi(\rho U) = \rho V_W^{inj} U_W^{inj} = \frac{\varphi^2}{\rho \sigma} \cotan(\alpha), \quad (18)$$

$$\Phi(\rho V) = \rho (V_W)^2 + P_{out}^{inj} = \frac{\varphi^2}{\rho} + P_{out}^{inj}, \quad (19)$$

$$\Phi(\rho W) = 0. \quad (20)$$

These fluxes are applied as boundary condition over the suction and the injection surfaces of the perforated plate. In this model, only a law for the discharge coefficient  $C_D$  and the geometrical characteristics of the plate  $(\alpha, \sigma)$  have to be provided by the user. The remainder of the calculus is done by the model, knowing the mass density  $\rho$  and the pressure at the wall grid points and at the first off-wall points.

### III. Presentation of the experimental configuration and of the LES code

#### A. Presentation of the LES Code

All simulations are carried out with the LES code developed at CERFACS, named AVBP ([www.cerfacs.fr/cfd/avbp\\_code.php](http://www.cerfacs.fr/cfd/avbp_code.php)). It is a cell-vertex/finite element code, explicit in time, which solves the compressible Navier–Stokes equations on unstructured meshes for the conservative variables (mass density, momentum and total energy). AVBP is dedicated to LES and DNS and has been widely used and validated in the past years in all kinds of configurations.<sup>29–32</sup> The computations presented in section IV deal with a case where the flow near the perforated wall is not well resolved. A coarse mesh is used in conjunction with the crudest numerical parameters available in AVBP: the sub-grid model is the classical Smagorinsky<sup>33</sup> model (with a constant fixed at  $C_S = 0.1$ ) and the numerical scheme for the large-scale simulations is the Lax-Wendroff scheme<sup>29</sup> (second order accurate in space and time).

#### B. The Experimental Configuration

All the calculations presented in this paper are related with a reference experiment named ‘LARA’<sup>18</sup> and performed at Turbomeca. The experimental set up allows to study the effusion process in the case of a large-scale isothermal configuration. The experimental test rig is divided into two channels: the first one, denoted by ‘1’, represents the combustion chamber side, with a primary flow of ‘hot gases’; the second one, denoted by ‘2’, represents the casing, with a secondary flow of ‘cooling air’ (Fig. 8). The two channels (height  $h = 120$  mm and width  $l = 400$  mm) are separated by a plate perforated with holes of diameter  $d = 5$  mm (0.5 mm is the common value for gas turbines). Twelve rows of staggered holes are drilled into the plate that separates the two channels. A grid is placed at the outlet section of channel 2 in order to generate a pressure drop across the plate. Because the pressure is

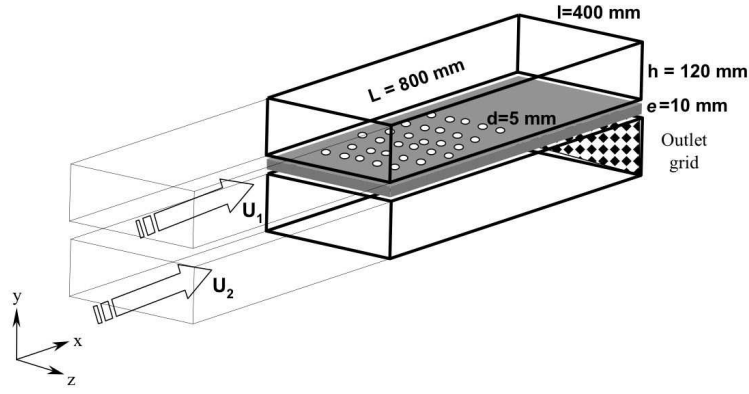


Figure 8. Principle of the large-scale isothermal LARA experiment.<sup>18</sup>

higher in the ‘casing side’, a fraction of the air flowing in channel 2 is injected through the perforated plate. The perforated plate characteristics are the same as in the reference small-scale simulation (see section II).

The following operating point has been considered: the pressure drop across the plate is  $\Delta P = 42$  Pa. The Reynolds number for the primary ‘hot’ flow (based on the duct centerline velocity  $U_1$  and the half height of the rectangular duct  $h/2$ ) is  $Re_1 = 17750$ , while it is  $Re_2 = 8900$  for the secondary ‘cold’ flow. The characteristics are given upstream of the perforated zone, where the flow is fully-developed. The Reynolds number in the hole, based on the momentum in the jet core at the hole exit and the hole diameter is  $Re_h = 2600$ . The ninth row has been chosen to compare with numerical results because it is the location where measurements are most numerous. Further details about this experiment can be found in studies by Miron<sup>34</sup> and Miron et al.<sup>18</sup>

#### IV. Validation of the uniform model in the LARA configuration

The model proposed in section II.B is implemented in the AVBP code (section IIIA) and tested in the case of the LARA experiment.<sup>18</sup> Figure 9 presents the computational domain of the large-scale large-eddy simulations performed for the *a posteriori* validation. It consists in two channels (height  $h = 0.12$  m and width 0.18 m) separated by a plate that is perforated over a streamwise distance of  $2.7h$ . The inflows are located  $6h$  upstream of the perforated part of the plate (referred as liner in Fig. 9). Fluid is injected through the liner from channel 2 to channel 1.

The side walls of the experiment have been replaced by periodic conditions in the spanwise direction  $z$ . In the simulation, the perforated part of the wall is replaced by the coupled boundary condition described in section II.C. The grid contains  $121 \times 31 \times 31$  hexahedral

nodes for channel 1 and  $121 \times 21 \times 31$  hexahedral nodes for channel 2. This difference is due to the lower value of Reynolds number imposed in channel 2 in the LARA experiment.

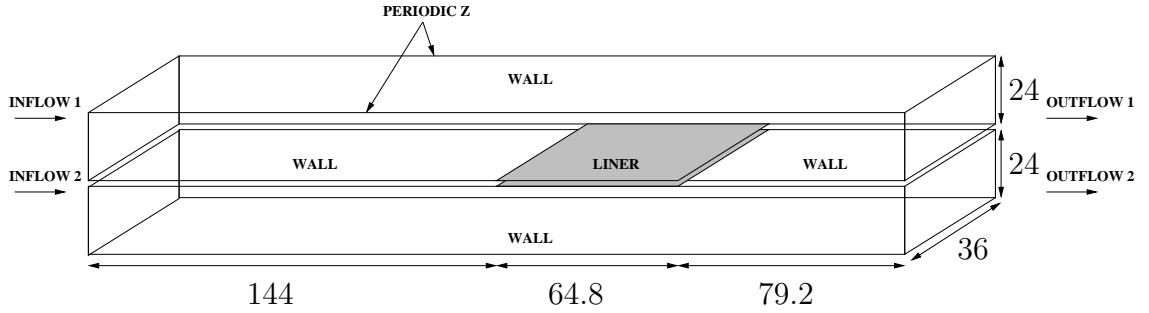


**Figure 9.** Large-scale computational domain for the *a posteriori* testing of the liner model. Dimensions are specified in hole diameters.

In the experiment, far enough from the side walls, the velocity profiles upstream of the perforated zone correspond to fully developed channel flow profiles. In the simulation, imposing the mean streamwise velocity profile at the inlet is not a satisfying approach: the flow needs a too long distance to destabilize and recover the characteristics of a fully turbulent channel. Thus it has been decided to accelerate this transition by using the Random Flow Generation (RFG) algorithm<sup>35,36</sup> to make the fluid velocity vary in time and space at the inlets. This method reproduces the effect of an incoming turbulent field thanks to the superposition of harmonic functions (100 modes projected along the three directions) with characteristic length-scales directly related to the geometry and the grid. This method has already been successfully employed in various simulations performed with AVBP.<sup>32,37</sup>

Ideally the fluctuating velocity profiles and the cross-correlation  $u_i u_j$  imposed at the simulation inlets should be the values measured in the experiment. However, in the LARA experiment, only a two-component laser-doppler anemometry system has been used and no data involving the spanwise component  $W$  is available. To overcome this problem, it has been decided to generate the characteristics of the inflow numerically. A periodic channel flow simulation with wall function boundary conditions is performed. The wall function boundary conditions have been developed in Schmitt *et al.*<sup>31</sup> in AVBP and validated in the case of a periodic channel flow; they used a logarithmic law to predict friction at the wall from the first off-wall point. Two periodic simulations have been performed to generate the statistics needed for the inflows of the top and bottom channels of the computational domain (Fig. 9). The size of the calculation domains in the periodic simulations is  $(3h, h, 2h)$ . Statistics (mean and fluctuating velocities, Reynolds stresses) are obtained from the time and spatial-averaging of eleven independent solutions. For consistency reasons, periodic simulations are performed with exactly the same parameters as the large-scale computation: the numerical parameters, grid spacing, spatial/temporal schemes, sub-grid scale model and wall function are identical.

The NSCBC method<sup>38</sup> is used for the inflow and outflow boundary conditions in the domain. The pressure at the outflows is imposed, with a pressure at outlet 2 (Fig. 9) superior to the one imposed at outflow 1 to ensure the injection of fluid from channel 2 to channel 1 through the model representing the perforated plate. The wall-function boundary conditions<sup>31</sup> are used for the solid walls in the large-scale computation, the first off-wall point being located approximately at  $y^+ = 45$ .

Computations have been run over 16 flow through times (FTT): the flow through time is based on the length of the channels and the crossflow velocity in channel 1,  $U_1$ . Time averages are accumulated over 8 FTT. In order to evaluate the quality of the model, it is compared to the most natural model for effusion cooling in which the perforated plate is replaced by a condition imposing the spatial-averaged velocity values at the wall, at the injection side. In other words, this condition conserves the mass flow rate and the aperture angle of the real plate. As a consequence, the model reads:

$$V = \sigma \frac{q}{S_h \rho} \quad \text{over} \quad S_W, \quad (21)$$

$$U = \sigma \frac{q}{S_h \rho} \cotan(\alpha) \quad \text{over} \quad S_W. \quad (22)$$

This simple model is referred to as Uniform Model 1 (UM1), the model presented in section II.B being denoted by UM2. Both models are identical on the suction side. Compared to UM2, UM1 imposes a streamwise velocity at the wall (and thus a streamwise momentum flux) lower of a factor  $\sigma$  (see Eq. 10).

Figures 10 and 11 present the time-averaged streamwise velocity field over the cutting plane  $z = 0$ , using respectively UM1 and UM2. As the treatment is identical for both models on the suction side, the main differences are observed in channel 1 (injection side). Both models do not influence the flow upstream of the perforated region ( $x < 144 d$ ). Results are thus zoomed over the region  $120 d < x < 288 d$ . In Fig. 10, the consequence of imposing a small streamwise momentum is observed, for  $x > 120 d$ : using UM1 induces a region of very low velocity near the perforated plate. This has a huge blocking effect on the main flow in channel 1: the passage area is reduced and the flow strongly accelerates. These effects are completely artificial and do not reproduce the reality of an effusion cooling configuration.<sup>16–18,34</sup>

Figure 11 shows a completely different behavior in channel 1. When reaching the perforated zone, the flow is modified in several ways: on the injection side, the flow is accelerated near the perforated plate due to positive streamwise momentum flux (1). Aft of the perforated region (2), the flow is accelerated in the center of channel 1. On the suction side, the flow is aspirated towards the plate, leading to higher streamwise velocity near the perforated plate (3). The effect of aspiration can also be seen near the bottom wall, where the velocity

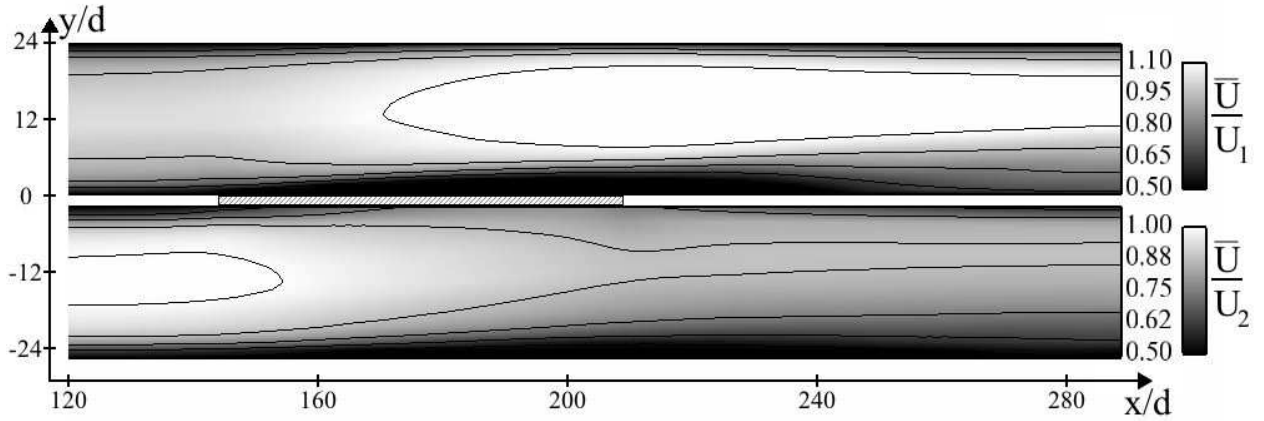


Figure 10. Field and isolines of time-averaged streamwise velocity over the cutting plane  $z = 0$  using model UM1. Zoom on the section between  $120 d < x < 288 d$ . Scale is different in each channel. In each channel,  $\bar{U}$  is divided by the velocity at the center of the channel:  $U_1$  for channel 1 and  $U_2$  for channel 2. The perforated part of the plate ( $144 d < x < 208.8 d$ ) is represented with a hatched rectangle.

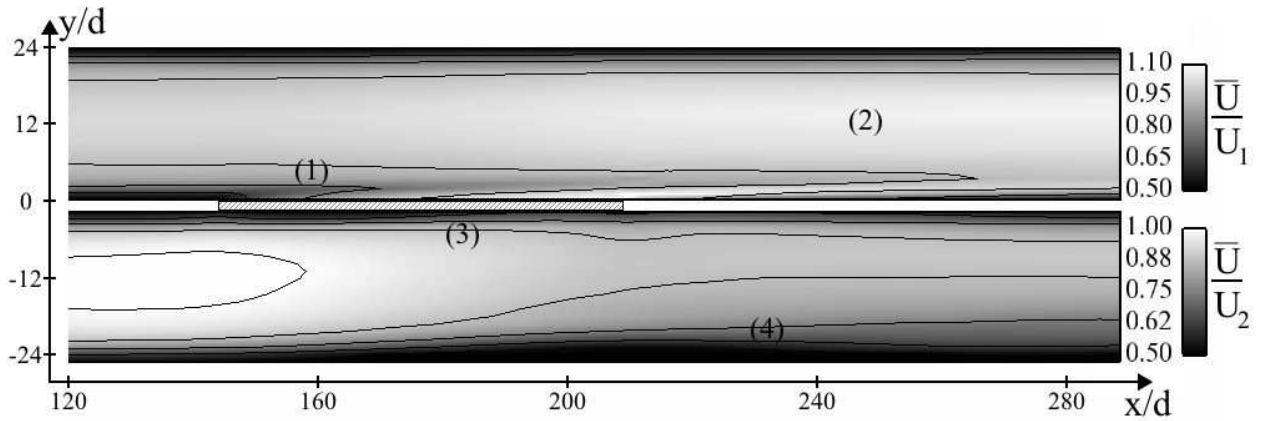
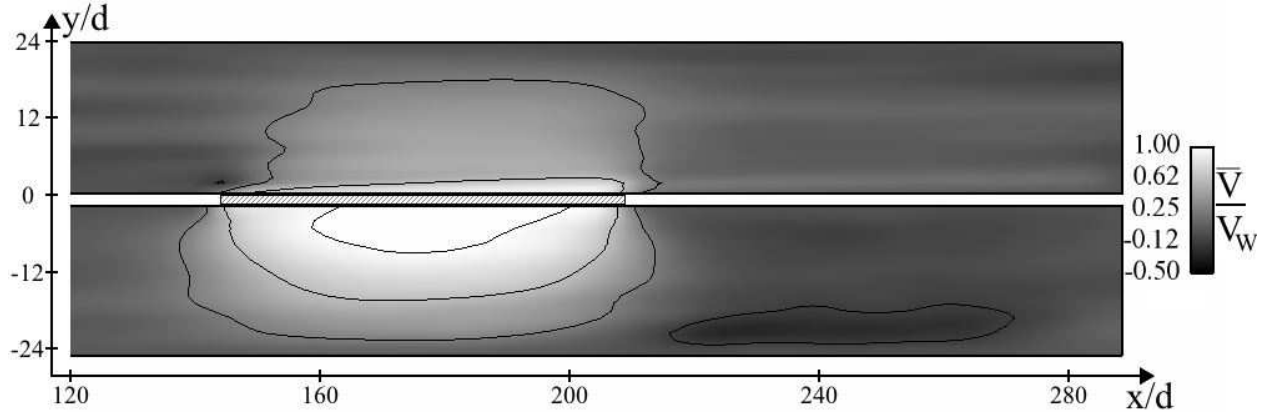


Figure 11. Field and isolines of time-averaged streamwise velocity over the cutting plane  $z = 0$  using model UM2. Zoom on the section between  $120 d < x < 288 d$ . Scale is the same as for Fig. 10. Zoom on the section between  $120 d < x < 288 d$ . The perforated part of the plate ( $144 d < x < 208.8 d$ ) is represented with a hatched rectangle.

decreases (4). This structure is similar to the one obtained by Mendez et al.<sup>26</sup>

The time-averaged vertical velocity is displayed in Fig. 12. Values are made dimensionless by dividing  $\bar{V}$  by  $V_W$ , the bulk vertical velocity at the perforated plate:  $V_W = \sigma \frac{q}{S_h \rho}$ . The time-averaged vertical velocity (see Fig. 12) is only disturbed near the perforated part of the plate. Downstream of this region, it recovers very small values. As expected, near the perforated plate the vertical velocity is approximately  $V_W$ , corresponding to the bulk vertical velocity.



**Figure 12.** Field and isolines of time-averaged vertical velocity field over the cutting plane  $z = 0$  using model UM2. Zoom on the section between  $120 d < x < 288 d$ .  $\bar{V}$  is divided by  $V_W$ , the bulk vertical velocity at the wall. The perforated part of the plate ( $144 d < x < 208.8 d$ ) is represented with a hatched rectangle.

In order to obtain a quantitative evaluation of the models, all the experimental profiles available for row 9 of the LARA experiment have been averaged for comparison with the numerical results. Eight experimental profiles are available at row 9, their locations being displayed by crosses in Fig. 13.

Experimental spatial-averaged profiles are calculated from these eight profiles. The four profiles located at  $z = 0$  are averaged together, then this profile is averaged with the other ones at  $z \neq 0$ . In other words, the eight experimental profiles are summed with a weight of 0.05 for the ones located at  $z = 0$  and 0.2 for the remaining ones ( $z \neq 0$ ). Of course, the resulting profile is only an approximation of the surface-averaged profile, used thereafter for comparison with numerical results. This comparison is shown in Fig. 14, from the wall to the center of channel 1 ( $0 < y < 12 d$ ). Numerical profiles are taken at  $z = 0$  and at  $x = 190.72 d$  ( $46.72 d$  from the beginning of the perforated zone): this corresponds to the distance between the holes of row 1 and row 9.

Streamwise velocity profiles are displayed in Fig. 14a. The experimental profile can be separated into two distinct regions: above  $y = 5 d$ , the velocity is not affected by effusion. On the contrary, near the plate, the profile is highly modified by effusion and shows a strong

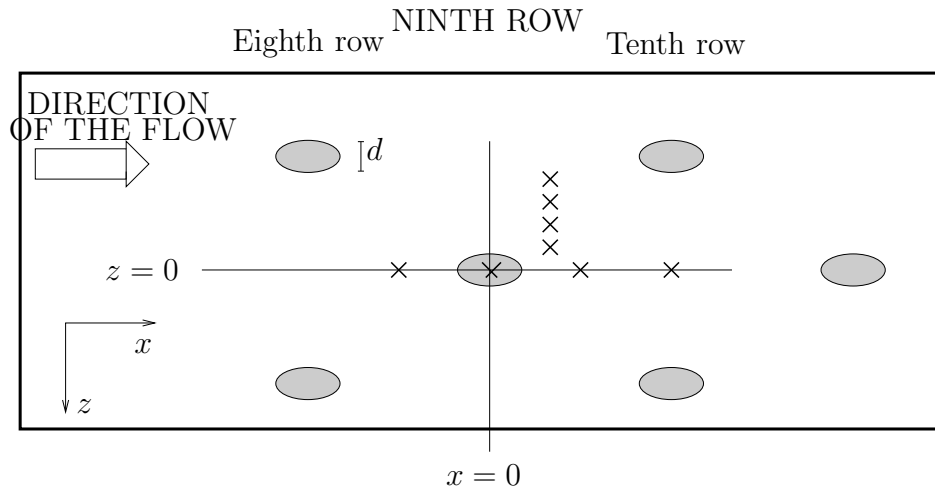


Figure 13. Zoom on the ninth row of the experimental test rig. The locations of the profiles measured in the experiment are represented by crosses.

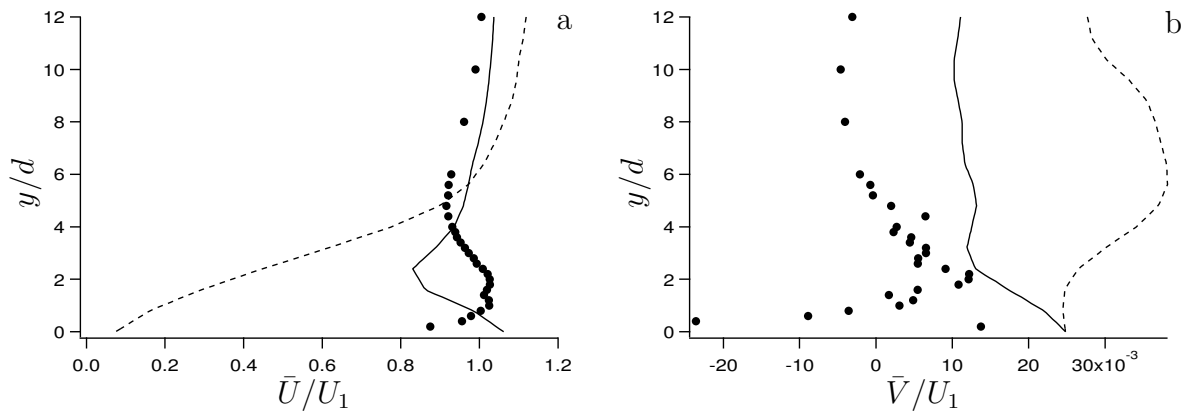


Figure 14. Evaluation of models UM1 ( ---- ) and UM2 ( ——— ). Numerical time-averaged velocity profiles at  $x = 190.72d$  and  $z = 0$  are compared to time- and spatial-averaged experimental data ( • ) at row 9. (a): streamwise velocity, (b): normal velocity.

acceleration. From Fig. 14a, the model UM2 is more appropriate than UM1. The wall velocity for the UM1 profile is very small and does not correspond at all with the experimental value. Moreover, this low-velocity condition has a blocking effect on the main flow: the passage area is reduced and the main flow accelerates above this region. On the contrary, the use of UM2 allows to obtain reasonable results: differences between experimental and numerical values using UM2 are of order of 10% (maximal errors are of order of 20%). Two types of discrepancies are observed: maximum values are observed near the wall. The model creates a zone of high velocity that accelerates the fluid above. However, due to uniform injection, the effect of the model is localized in the vicinity of the wall ( $y < 2d$ ). On the other hand, the flow slightly accelerates above the film region ( $y > 4d$ ). This effect is much weaker using UM2 than UM1 but it exists in both cases.

Figure 14b displays the vertical velocity profiles. It is much more difficult to conclude on this figure. Eight profiles are not sufficient to obtain a satisfying measure of the spatially-averaged vertical velocity: numerical simulations inject the good mass flow rate through the plate (the discharge coefficient is known from the small-scale LES) so at least the values near the perforated wall should be close to the ones obtained in the simulations.

These calculations have shown the ability of model UM2 to reproduce a structure of the flow that presents satisfactory results by comparison with the LARA experimental database. Of course, the results are not perfect, but they are considered to be satisfactory, given the simplicity of the model. As could be guessed after the flux analysis in section II, the model UM1 injects a very small streamwise momentum flux. As a consequence, the resulting flow is completely different from the one observed experimentally. Differences between experimental and numerical results are observed near the perforated plate, due to an under-estimation of the streamwise momentum flux. Note also that for a better validation of the model, detailed experimental data are needed, ideally providing spatially-averaged velocity profiles.

## V. Conclusion

In this paper, an adiabatic model to account for multi-perforated liners in combustion chamber flow simulations is described. It is separated into a suction model and an injection model to account for the effect of effusion at both sides of the plate. The modeling respects two important constraints: the model is local and homogeneous. By local we mean that the effect of effusion through the perforated plate is assessed only from local quantities, without any reference to global parameters such as the distance to the edge of the perforated zone for example. It is homogeneous because it does not impose any constraint in terms of grid size at the wall: the perforated plate is replaced by a homogeneous boundary condition on which the model is applied.

Mendez *et al.*<sup>25,27</sup> have performed wall-resolved Large-Eddy Simulations of the flow around a multi-perforated plate in an isothermal case. The analysis of these results show that if the mass flow rate through the plate is known, the difficult task is to assess the streamwise momentum flux. It is also shown that the main contribution to the streamwise momentum flux is due to the inviscid injection of fluid through the hole: wall friction over the solid wall is approximately ten times smaller. This paper presents a way to reproduce at least the inviscid part of the streamwise momentum flux at the perforated wall.

The model is built in two steps. First, the velocity fields at the hole inlet/outlet are approximated by constant values. Then, two homogeneous models are constructed from these approximated fields, conserving either the spatially-averaged velocities (UM1) or fluxes at the wall (UM2). Both models are implemented in an LES code. They are tested by reproducing the experimental configuration of two channel flows separated by a plate including a perforated region. The experimental perforated zone is replaced by the numerical homogeneous model. The two sides of the plate are coupled, the mass flow rate being not imposed but calculated locally from the local pressure drop and from the perforated plate geometry. From the comparisons with spatially-averaged experimental data, the model built to reproduce the wall fluxes (UM2) is the best one. UM1 imposes a very low streamwise velocity at the wall, which is not observed in the experiment. On the contrary, the global behavior of the flow seems to be correctly reproduced using model UM2. Moreover, reasonable agreement with experimental data is obtained on streamwise velocity profile in the perforated zone. Velocity levels are globally satisfactory, even if neglecting the wall friction leads to obtain the maximum velocity at the wall. The model proposed in this paper can be considered as a good candidate to account for multi-perforated plates when computing the flow in complex systems, without resolving the details of the flow around the plates.

Reference small-scale simulations have been used not only to determine which physical effects (viscous or non-viscous terms, for example) have to be modeled but also to evaluate the exactness of the modeling assumptions. The comparison with the reference small-scale wall-resolved LES data indicates that improvements to the UM2 model can be obtained by refining the modeling of the spatial-averaged streamwise velocity at the hole inlet/outlet and by accounting for the shape of the time-averaged velocity field at the hole inlet/outlet.

## Acknowledgments

The authors are grateful to the European Community for funding this work under the project INTELLECT-DM (Contract No. FP6 - AST3 - CT - 2003 - 502961), and to the CINES (Centre Informatique National pour l'Enseignement Supérieur) and the BSC (Barcelona Supercomputing Center) for the access to supercomputer facilities. The authors

would also like to thank Turbomeca and Petre Miron for the access to the LARA experimental database.

## References

- <sup>1</sup>Lefebvre, A. H., *Gas Turbines Combustion*, Taylor & Francis, 1999.
- <sup>2</sup>Simpson, R. L., “Characteristics of turbulent boundary layers at low Reynolds numbers with and without transpiration,” *Journal of Fluid Mechanics*, Vol. 42, No. 4, 1970, pp. 769–802.
- <sup>3</sup>Piomelli, U., Ferziger, J. H., Moin, P., and Kim, J., “New approximate boundary conditions for large eddy simulations of wall-bounded flows,” *Physics of Fluids A*, Vol. 1, No. 6, 1989, pp. 1061–68.
- <sup>4</sup>MacManus, D. G. and Eaton, J. A., “Flow physics of discrete boundary layer suction - measurements and predictions,” *Journal of Fluid Mechanics*, Vol. 417, 2000, pp. 47–75.
- <sup>5</sup>Peterson, S. D. and Plesniak, M. W., “Evolution of jets emanating from short holes into crossflow,” *Journal of Fluid Mechanics*, Vol. 503, 2004, pp. 57–91.
- <sup>6</sup>Peet, Y. V., *Film cooling from inclined cylindrical holes using Large-Eddy Simulations*, Ph.D. thesis, Stanford University, 2006.
- <sup>7</sup>Margason, R. J., “Fifty years of jet in crossflow research,” *Computational and Experimental Assessment of Jets in Crossflow*, edited by U. Winchester, Vol. AGARD-CP-534, 1993, pp. 1–41.
- <sup>8</sup>Eric, T. and Roshko, A., “Vortical structure in the wake of a transverse jet,” *Journal of Fluid Mechanics*, Vol. 279, 1994, pp. 1–47.
- <sup>9</sup>Smith, S. H. and Mungal, M. G., “Mixing, structure and scaling of the jet in crossflow,” *Journal of Fluid Mechanics*, Vol. 357, 1998, pp. 83–122.
- <sup>10</sup>Cortelezzi, L. and Karagozian, A. R., “On the formation of the counter-rotating vortex pair in transverse jets,” *Journal of Fluid Mechanics*, Vol. 446, 2001, pp. 347–373.
- <sup>11</sup>Muppidi, S. and Mahesh, K., “Direct Numerical Simulation of round turbulent jets in crossflow,” *Journal of Fluid Mechanics*, Vol. 574, 2007, pp. 59–84.
- <sup>12</sup>Bergeles, G., Gosman, A. D., and Launder, B. E., “The Near-Field Character of a Jet Discharged Normal to a Main Stream,” *Journal of Heat Transfer*, 1976, pp. 373–378.
- <sup>13</sup>Bergeles, G., Gosman, A. D., and Launder, B. E., “Near-Field Character of a Jet Discharged through a Wall at 30 deg to a Mainstream,” *AIAA Journal*, Vol. 15, No. 4, 1977, pp. 499–504.
- <sup>14</sup>Iourokina, I. V. and Lele, S. K., “Large Eddy Simulation of Film-Cooling Above the Flat Surface with a Large Plenum and Short Exit Holes,” *44th Aerospace Sciences Meeting and Exhibit*, 2006.
- <sup>15</sup>Walters, D. and Leylek, J., “A Detailed Analysis of Film-Cooling Physics: Part 1- Streamwise Injection With Cylindrical Holes,” *Journal of Turbomachinery*, Vol. 122, 2000, pp. 102–112.
- <sup>16</sup>Yavuzkurt, S., Moffat, R. J., and Kays, W. M., “Full coverage film cooling. Part 1. Three-dimensional measurements of turbulence structure,” *Journal of Fluid Mechanics*, Vol. 101, 1980, pp. 129–158.
- <sup>17</sup>Gustafsson, K. M. B., *Experimental Studies of Effusion Cooling*, Ph.D. thesis, Chalmers University of Technology. Göteborg, 2001.
- <sup>18</sup>Miron, P., *Étude expérimentale des lois de parois et du film de refroidissement produit par une zone multiperforée sur une paroi plane.*, Ph.D. thesis, Université de Pau et des Pays de l’Adour, 2005.
- <sup>19</sup>Metzger, D. E., Takeuchi, D. I., and Kuenstler, P. A., “Effectiveness and heat transfer with full-coverage film-cooling,” *ASME paper*, 1973.
- <sup>20</sup>Crawford, M. E., Kays, W. M., and Moffat, R. J., “Full-coverage film cooling. Part I: Comparison of Heat Transfer Data for Three Injection Angles,” *Journal of Engineering for Power*, Vol. 102, 1980, pp. 1000–1005.

- <sup>21</sup>Bazdidi-Tehrani, F. and Andrews, G. E., “Full-coverage discrete hole film cooling: investigation of the effect of variable density ratio,” *Journal of Engineering for Gas Turbines and Power*, Vol. 116, 1994, pp. 587–596.
- <sup>22</sup>Rouvreau, S., *Étude expérimentale de la structure moyenne et instantanée d’un film produit par une zone multiperforée sur une paroi plane. Application au refroidissement des chambres de combustion des moteurs aéronautiques*, Ph.D. thesis, E.N.S.M.A. et Faculté des Sciences Fondamentales et Appliquées, 2001.
- <sup>23</sup>Hay, N. and Lampard, D., “Discharge Coefficient of Turbines Cooling Holes,” *Journal of Turbomachinery*, Vol. 120, 1998, pp. 314–319.
- <sup>24</sup>Gritsch, M., Schultz, A., and Wittig, S., “Effect of Crossflows on the Discharge Coefficient of Film Cooling Holes With Varying Angles of Inclination and Orientation,” *Journal of Turbomachinery*, Vol. 123, 2001, pp. 781–787.
- <sup>25</sup>Mendez, S., Nicoud, F., and Poinso, T., “Large-Eddy Simulations of a Turbulent Flow around a Multi-Perforated Plate,” In *Complex effects in LES*, Vol. 56, 2006, pp. 289–303.
- <sup>26</sup>Mendez, S., Eldredge, J. D., Nicoud, F., Poinso, T., Shoeybi, M., and Iaccarino, G., “Numerical investigation and preliminary modeling of a turbulent flow over a multi-perforated plate,” *Proceedings of the Summer Program*, Center for Turbulence Research, NASA AMES, Stanford University, USA, 2006.
- <sup>27</sup>Mendez, S. and Nicoud, F., “Large-eddy simulation of a bi-periodic turbulent flow with effusion,” *Journal of Fluid Mechanics*, Vol. 598, 2008, pp. 27–65.
- <sup>28</sup>Mayle, R. and Camarata, F., “Multihole cooling effectiveness and heat transfer,” *Journal of Heat Transfer*, Vol. 97, 1975, pp. 534–538.
- <sup>29</sup>Schönfeld, T. and Rudgyard, M., “Steady and unsteady flows simulations using the hybrid flow solver AVBP,” *AIAA Journal*, Vol. 37, No. 11, 1999, pp. 1378–1385.
- <sup>30</sup>Moureau, V., Lartigue, G., Sommerer, Y., Angelberger, C., Colin, O., and Poinso, T., “Numerical methods for unsteady compressible multi-component reacting flows on fixed and moving grids,” *Journal of Computational Physics*, Vol. 202, No. 2, 2005, pp. 710–736.
- <sup>31</sup>Schmitt, P., Poinso, T., Schuermans, B., and Geigle, K., “Large-eddy simulation and experimental study of heat transfer, nitric oxide emissions and combustion instability in a swirled turbulent high-pressure burner,” *Journal of Fluid Mechanics*, Vol. 570, 2007, pp. 17–46.
- <sup>32</sup>Prière, C., Gicquel, L. Y. M., Kaufmann, A., Krebs, W., and Poinso, T., “LES predictions of mixing enhancement for jets in cross-flows,” *Journal of Turbulence*, Vol. 5, 2004, pp. 005.
- <sup>33</sup>Smagorinsky, J., “General circulation experiments with the primitive equations: I. The basic experiment,” *Monthly Weather Review*, Vol. 91, 1963, pp. 99–164.
- <sup>34</sup>Miron, P., Bérat, C., and Sabelnikov, V., “Effect of blowing rate on the film cooling coverage on a multi-holed plate: application on combustor walls,” *Eighth International Conference on Heat Transfer. Lisbon, Portugal*, 2004.
- <sup>35</sup>Celik, I., Smirnov, A., and Smith, J., “Appropriate initial and boundary conditions for LES of a ship wake,” *Proceedings of the 3rd ASME/JSME Joint Fluids Engineering Conference*, Vol. FEDSM99-7851, San Francisco, California, USA, 1999.
- <sup>36</sup>Smirnov, A., Shi, S., and Celik, I., “Random Flow Generation Technique for Large Eddy Simulations and Particle-dynamics Modelling,” *J. of Fluids Engineering*, Vol. 123, 2001, pp. 359–371.
- <sup>37</sup>Riber, E., García, M., Moureau, V., Pitsch, H., Simonin, O., and Poinso, T., “Evaluation of numerical

strategies for LES of two-phase reacting flows,” *Proceedings of the Summer Program*, Center for Turbulence Research, NASA AMES, Stanford University, USA, 2006, pp. 197–211.

<sup>38</sup>Poinsot, T. and Lele, S. K., “Boundary conditions for direct simulations of compressible viscous flows,” *Journal of Computational Physics*, Vol. vol.101, No. 1, 1992, pp. 104–129.